Difference in anisotropic vortex pinning in pristine and proton-irradiated $(Ca_{0.85}La_{0.15})_{10}(Pt_3As_8)(Fe_2As_2)_5$ single crystals

W.J. Choi [a,b,1], Y.I. Seo [a,1], K. Park [a], Yong Seung Kwon [a,*]

[a] *Department of Emerging Materials Science, DGIST, Daegu 711-873, Republic of Korea*
[b] *Emerging Materials Science Research Center, DGIST, Daegu 711-873, Republic of Korea*

A B S T R A C T

We measured the in-plane electrical resistivity of pristine and irradiated $(Ca_{0.85}La_{0.15})_{10}(Pt_3As_8)(Fe_2As_2)_5$ single crystals in $B//c$ and $B//ab$ up to $B = 13$ T to study the difference between in-plane and out-of-plane vortex pinning and the effect of proton irradiation on these pinning. The crystal structure analyzed by the selected area electron diffraction was monoclinic in these two samples. Protons incident along the c-axis caused an expansion of the lattice constants a and b. The expansion of the lattice constants significantly increased the c-axis coherence length ξ_c. The vortex pinning in $B//ab$ is well understood by an intrinsic pinning mechanism, which was attenuated by proton irradiation. On the other hand, the vortex pinning in $B//c$ is well understood by the plastic creep theory due to point defects that are enhanced by proton irradiation.

Introduction

The limitation to technological advances in iron-based superconductors essentially comes from the low critical current density J_c. Since J_c is in many cases limited by thermally activated vortex motion, the most important way to increase J_c is to introduce pinning centers for vortices into the superconductor during or after sample preparation [1]. Therefore, it is very important for superconductor applications to know how to change the vortex pinning energy to be controllable in the process of maximizing J_c.

In vortex pinning of iron-based superconductors, various types of defects naturally occurring during sample preparation play a major role. These defects include atomic defects (vacancies, impurities, etc.) and structural defects (twin boundaries, stacking faults, dislocations and grain boundaries, etc.) in iron-based superconductors [2–6]. The pinning center can also be introduced by artificially irradiating high energy particles, and the resulting defects can vary in shape from point defects to columnar defects [7–9]. The biggest advantage of using particle irradiation is that it can generate defects at a precisely controlled concentration, allowing us to explore the relationship between pinning energy and defect concentration or defect type.

In a layered superconductor with high anisotropy a magnetic field parallel to the layers carries a large critical current density at low temperatures, and this current density persists up to a high magnetic field [10–13]. These results arise from the strong inhibition of vortex parallel to the layers from moving perpendicular to the layers. Many groups have proposed intrinsic pinning to understand this pinning [14–18]. Intrinsic pinning results from two effects: One is that the strong superconducting layer acts as a potential barrier to vortices moving perpendicular to the layer, and the other is that the transport current density flowing in the weak superconducting layer reduces the driving force for the vortex moving perpendicular to the layer. Intrinsic pinning was observed in cuprate superconductors with large anisotropy [10–13], but not even in REFeAsO$_{1-x}$F$_x$ (RE = rare-earth elements), which has the highest anisotropy in iron-based superconductors.

The parent $Ca_{10}(Pt_3As_8)(Fe_2As_2)_5$ (herein called Ca 10–3–8) compound is semiconducting, not like a typical iron-based superconductor, and is ordered antiferromagnetically without further reduction in crystal symmetry at $T_N \sim 110$ K. The doping effect in the parent compound leads to superconductivity [19]. The electron doping effect of replacing Ca site with La raises the superconducting temperature to $T_c \sim 35$ K [20], but the electron doping effect replacing Fe site with Pt raised T_c to 13 K [21], which is reduced. The parent compound has multiple Fermi surfaces like other FeAs superconductors, and the subtle difference between these Fermi surfaces induces superconductivity at $T_c = 8$ K without doping [22].

The Ca 10–3–8 family has a stacked crystal structure with Ca-(Pt_3As_8)-Ca-(Fe_2As_2) layers, where the Ca layer serves as a reservoir layer for supplying electric charges to the Fe_2As_2 layer, and the Pt_3As_8 layer serves as an intermediate layer controlling the distance between the Fe_2As_2 layers [23]. This crystal structure is similar to the oxide superconductor $Bi_2Sr_2Ca_{n-1}Cu_nO_{2n+4+x}$ (BSCCO) with an intermediate layer [24]. It was suggested that the high T_c in BSCCO resulted from enhanced CuO_2 layer coupling through the intermediate layer [25–27]. In this context, the Ca 10–3–8 family is one of the good candidates to study T_c enhancement in FeAs-superconductors.

For the study of T_c enhancement as well as the delicate relationship between electronic structure and superconductivity, many experiments such as transport [23,28], APRES [22,29], pressure effect [30], infrared spectroscopy [31–33], upper critical field [21,28,34], penetration depth [35,36] and thermally activated flux motion (TAFM) [37] have been performed. Recently, TAFM experiments [37] have already been performed for La-doped Ca 10–3–8 in the $B//c$-axis direction up to $B = 6$ T. The result of TAFM analysis for this experiment showed the magnetic field dependence of $U_0 \sim B^{-1.11}$ on the zero-temperature activation energy in the entire measured magnetic field region, which was suggested to be due to the entanglement of vortex lines pinned to the point defect. To understand this more clearly in this paper, we performed TAFM experiments in two directions of $B//c$-axis and $B//ab$-plane up to 13 T for $Ca_{8.5}La_{1.5}(Pt_3As_8)(Fe_2As_2)_5$ single crystal. In addition, the TAFM experiment was performed under the same conditions in the $Ca_{8.5}La_{1.5}(Pt_3As_8)(Fe_2As_2)_5$ single crystal irradiated with protons.

For the $B//c$-axis, both pristine and irradiated samples showed magnetic field dependence on the zero-temperature activation energy of the form $U_0 \sim B^{-1.20\sim1.21}$, similar to previously reported results [37], and interestingly, the magnitude of U_0 in the irradiated sample increased over the entire magnetic field region compared to the pristine sample, indicating that the main vortex pinning on the $B//c$-axis is due to point defects. On the other hand, for the $B//ab$-plane, the magnetic field dependence on the zero-temperature activation energy deviated from the form $U_0 \sim B^{-\alpha}$ and the magnitude of U_0 increased significantly compared to the $B//c$-axis, indicating that vortex pinning is due to intrinsic pinning different from the pinning in $B//c$.

Experimental details

$(Ca_{0.85}La_{0.15})_{10}(Pt_3As_8)(Fe_2As_2)_5$ single crystals were grown by a Bridgman method. In order to accurately make a compound of the desired molar ratio with arsenic having a gaseous phase and Ca, La, Pt, and Fe having a liquid phase at high temperature, the precursors of CaAs, LaAs and FeAs was synthesized at 550, 800 and 1050 °C in evacuated quartz ampoules, respectively. The powdered precursors and Pt element were mixed in a mortar and then placed in a BN crucible. In order to prevent the evaporation of each element, especially arsenic, into a vapor state at high temperature, the filled BN crucible was put into a Mo-crucible and covered with a lid, and the contact part between the crucible and the lid was welded in a high purity Ar-gas atmosphere using an arc welding machine. The welded Mo-crucible was placed in an electric furnace with a tungsten mesh heater with ±0.1 °C temperature stability, and a single crystal was grown at 1250 °C.

Proton irradiation along the c-axis of the single crystal was performed at 300 K using an MC-50 cyclotron installed at KIRAM (Korea institute of radiological & medical sciences). The proton energy is 3 MeV and the total dose of the incident proton is 5×10^{15} cm^{-2}. To prevent the temperature-rise of the sample during proton irradiation, we fixed the specimen to a water copper block and used a weak proton dose rate of $\sim 2 \times 10^{11}$ cm$^{-2} \cdot$s^{-1}. The thickness of the sample for proton irradiation is ~ 40 μm, simulated with the SRIM program for perfect projection [38].

The in-plane electrical resistivity in $B//c$ and $B//ab$ using grown single crystals were measured by the four-probe method at a current density of about 20 A/cm^2 using the Oxford superconducting system. The gold wires were attached to the sample electrodes using silver epoxy

(EPO-TEK H20E). Gold was deposited in advance on the sample surface for the probes to reduce the contact resistance below 1 Ω. The electrical resistivity was measured from 2 to 85 K with $B = 0.5, 1, 2, 3, 5, 7, 9, 11$ and 13 T.

The X-ray diffraction experiments were performed using a PANalytical X-ray powder diffractometer with Cu Kα radiation (40 kV, 30 mA and $\lambda = 1.5406$ Å) at step size of 0.026° (2θ) and scan rate of 0.78°/min.

Selected area electron diffraction (SAED) patterns were measured at 300 kV accelerating voltage using a high-resolution transmission electron microscope (HR-TEM, Hitachi HF-3300). As a pretreatment process for HR-TEM, the thickness of all samples was processed to less than 100 nm using a dual-beam focused ion beam (dual-beam FIB, Hitachi NB 5000) under an acceleration voltage of 40 kV. To analyze the SAED pattern, the ReciPro program was used. All spots of the pattern were fitted with the ReciPro program to obtain d-spacing of the sample and the angle between the spots [39]. From these fitting results, we found a pattern that closely matches the experimental SAED pattern based on the crystal structures and space groups of Ca 10–3–8 [40] and $Ca_{10}(Pt_4As_8)(Fe_2As_2)_5$ (herein called Ca 10–4–8) [41], which are known to date. The lattice constants of all samples were obtained by refinement using UNITCELL software [42]. The simulated SAED pattern was obtained using dynamical theory and simulated by adjusting both the Bloch waves and thickness parameters.

Results and discussion

XRD and SAED analysis

The XRD results for pristine and irradiated $(Ca_{0.85}La_{0.15})_{10}(Pt_3As_8)$ $(Fe_2As_2)_5$ single crystals are shown in Fig. 1. In both samples, only $(00\,l)$-oriented peaks were observed, which indicates that the direction of the incident X-ray is parallel to the c-axis and that the measured sample is a single phase without a secondary phase. Each peak position was the same within the error in the two samples, indicating that the estimated interplanar distance in the two samples was equal to 10.37 Å. This value is almost consistent with the results reported for pristine samples [28]. As shown in the inset of Fig. 1, the FWHM (the full width at half maximum) of the pristine sample and the irradiated sample is evaluated at a very narrow 0.029° and 0.035°, respectively. This indicates that the pristine single crystal was aligned with almost no structural defects, and that the proton irradiated single crystal had slightly more structural defects than the pristine sample.

We performed crystal structure analysis by selected area electron diffraction (SAED) method using transmission electron microscopy (TEM) to find crystallographic changes between pristine and proton irradiated $(Ca_{0.85}La_{0.15})_{10}(Pt_3As_8)(Fe_2As_2)_5$ single crystals. Fig. 2(a), 2 (b) and 2(c), 2(d) show the experimental results of the SAED analysis for the zone axes [0 0 1] and [0 1 0] in pristine and proton-irradiated single crystals, respectively. These two patterns for both samples do not show a ring pattern at the center point, indicating that both samples are almost perfect single crystals with no polycrystalline components. Moreover, the defects induced by proton irradiation did not cause a distinct change in the SAED diffraction patterns and could not be identified even in cross-sectional TEM images within the nanoscale. Interestingly, as will be discussed below, these two results were not explained by the patterns obtained using the lattice parameters and spatial groups of triclinic structures previously reported [40]. Instead, this measured SAED pattern is well described as a monoclinic structure with a spatial group of P2$_1$/n, which is similar to the recently published pattern of γ-$Ca_{10}(Pt_4As_8)(Fe_2As_2)_5$ (herein called γ-Ca 10–4–8) [41].

La-doped $Ca_{10}(Pt_3As_8)(Fe_2As_2)_5$ cannot have a Pt_4As_8 layer as confirmed by EDS analysis using TEM. According to the results of the triclinic structure La-doped $Ca_{10}(Pt_3As_8)(Fe_2As_2)_5$, the location of the La atom in the unit cell is located just above and below the Pt vacancies in the $Pt_3\square As_8$ layer [40]. Here, $\square$ means Pt vacancy. La^{3+}, which has a
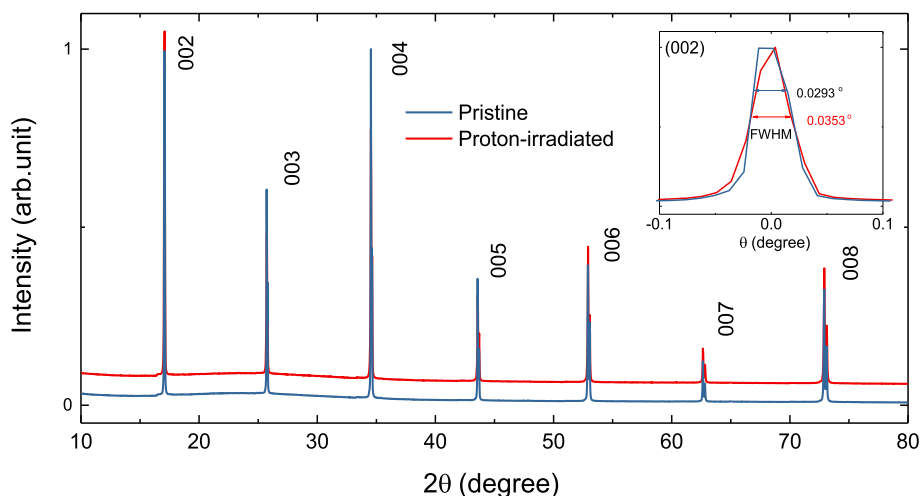
Fig. 1. XRD patterns for pristine and irradiated $(Ca_{0.85}La_{0.15})_{10}(Pt_3As_8)(Fe_2As_2)_5$ single crystals. The inset showed an extended (002) peak for the determination of full width at half maximum (FWHM).

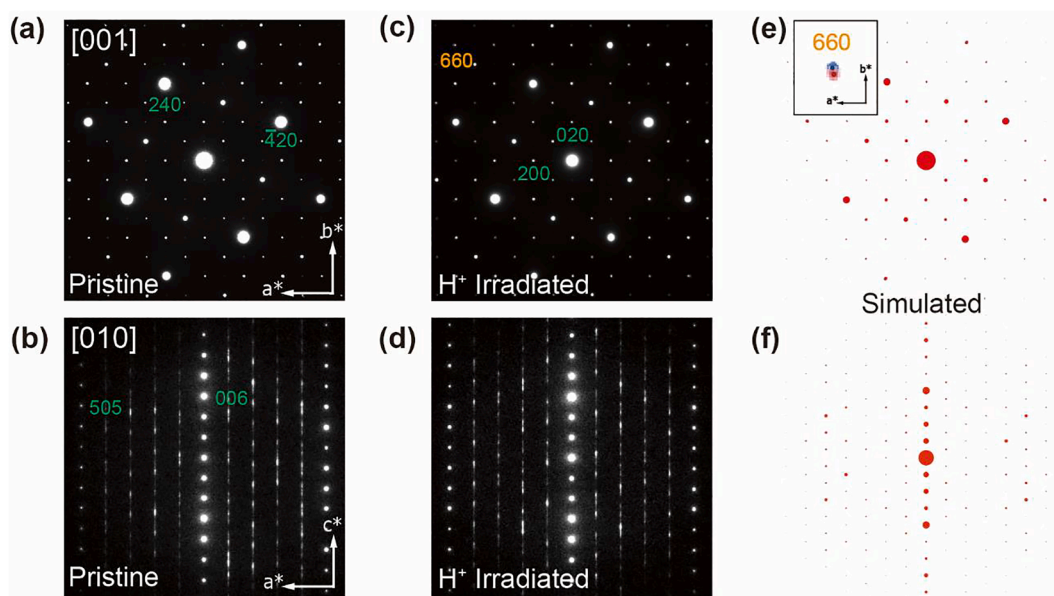**Fig. 2.** (a) and (b) are experimental electron diffraction patterns for the [001] and [010] directions in the pristine $(Ca_{0.85}La_{0.15})_{10}(Pt_3As_8)(Fe_2As_2)_5$ single crystal, respectively. (c) and (d) are experimental electron diffraction patterns for the [001] and [010] directions in the irradiated $(Ca_{0.85}La_{0.15})_{10}(Pt_3As_8)(Fe_2As_2)_5$ single crystal, respectively. (e) and (f) are simulated electron diffraction patterns in [001] and [010] directions, respectively, where the blue is for the pristine sample and the red circle is for the irradiated sample. The inset of (e) is the diffraction spot at Miller index (660): large circles are experimentally measured and small dots are theoretically calculated points. (For interpretation of the references to color in this figure legend, the reader is referred to the web version of this article.)

higher charge than Ca^{2+}, is known to prefer this site by lowering its lattice energy when it is located directly above and below the Pt vacancy [40]. In our compound, the La atom is located almost near the Pt vacancies in the $Pt_3\square As_8$ layer, which is expected to have a similar structure to the Pt_4As_8 layer structure, resulting in a change from triclinic to monoclinic crystal structure. In order to obtain more accurate information on the atomic position of the crystal structure, additional experiments with single crystal XRD or high-angle annular dark-field scanning transmission electron microscopy (HAADF-STEM) are required. In the SAED pattern, diffused stripes appear along the zone axis [010]. These diffused stripes would have been caused by un-avoidable sample cross-section damage due to Focused Ion Beam (FIB) in the TEM pretreatment of $(Ca_{0.85}La_{0.15})_{10}(Pt_3As_8)(Fe_2As_2)_5$ with a layered structure.

Fig. 2(e) and 2(f) show simulated SAED patterns of pristine and irradiated samples for each zone axis, respectively. The blue color spot

represents the simulated SAED pattern for the pristine sample, and the red color one represents the proton irradiated sample. As in the figures, the two spots almost overlap over a large area of the reciprocal lattice, so the two spots are hardly distinguished. However, in Fig. 2(e), an enlarged view for the spot diffracted from the Miller index (660), there is a clear difference between the location of the blue spot for the pristine sample and the location of the red spot for the proton irradiated sample. This small difference arises from the difference in small lattice constants between the two samples. These theoretical simulations agree well with the experimental results indicated by large circles, as shown in the inset in Fig. 2(e). The lattice parameters for the pristine and irradiated samples were obtained by performing simulations on the SAED pattern of each zone axis. The lattice parameters a and b were obtained from the zone axis [001] of each sample, and the lattice parameters a and c were obtained from the zone axis [010]. The lattice parameter a obtained from the zone axis [001] and [010] of each sample was the same. From

the results of the simulated pattern, the lattice parameter of the pristine sample was evaluated as $a = 8.727 \pm 0.0122$, $b = 8.776 \pm 0.0096$, $c = 20.800 \pm 0.0083$ Å, $\gamma = 89.05 \pm 0.035°$, and the lattice parameter of the proton irradiated sample was evaluated as $a = 8.764 \pm 0.0087$, $b = 8.829 \pm 0.0088$, $c = 20.800 \pm 0.0042$ Å, $\gamma = 89.85 \pm 0.026°$. In other words, the lattice parameters a and b for the proton irradiated sample increase by 0.42 and 0.60%, respectively, compared to the pristine sample, but the lattice parameter c does not change. This is a very interesting result. The difference in the constants for the lattice between the two samples was very small, but it was certainly larger than the error for each. The interlayer distance obtained by XRD is obtained by assuming a triclinic structure, but as discussed above, the crystal structure of this compound is a monoclinic structure as a result of SAED analysis. The crystal structure of Ca 10–3–8 has been reported as a triclinic structure [23,40,43]. The lattice parameter c reportoed by Ni et al. [23] and Stürzer et al. [40] are 10.641 Å and 10.7139 Å, respectively. However, the c value reported by Kakiya et al. [43] is 21.008 Å, which is twice that of the other two groups. Interestingly, our optimally La doped sample is similar to the lattice parameter by Kakiya et al., but has a monoclinic structure. In the case of Ca 10–4–8, which can be compared with the structure of our samples, various crystal structures exist in triclinic [43], monoclinic [41], and tetragonal [23] structures depending on the growth method and environment. According to the reported γ-Ca 10–4–8 compound, the unit cell of the monoclinic structure is a super cell having twice the size of the lattice constant of the c-axis in the triclinic structure (by Ni et al. and Stürzer et al.) [41]. Therefore, the interlayer distance obtained by XRD is modified to 20.74 Å in a monoclinic structure. This value is similar to the value of the lattice parameter c of the sample obtained from the result of the simulated pattern.

Electrical resistivity in zero magnetic field

The in-plane electrical resistivity near T_c for pristine and irradiated $(Ca_{0.85}La_{0.15})_{10}(Pt_3As_8)(Fe_2As_2)_5$ single crystals at $B = 0$ is shown in Fig. 3. The abrupt decrease to zero electrical resistivity due to the superconducting transition is observed in both samples. In the normal state, the electrical resistivity slowly bends downward as the temperature approaches T_c. Similar behavior was observed in La/Pt-underdoped Ca 10–3–8 sampl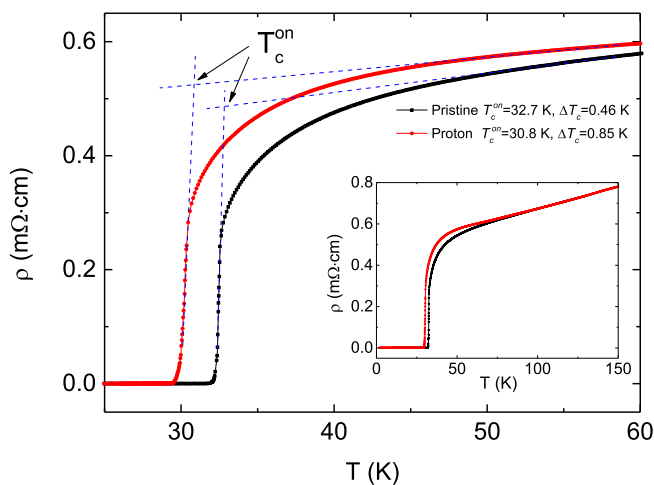es [21,28,32]. As can be seen in the inset, the normal-state electrical resistivity of the irradiated sample compared to the pristine sample is large just above T_c, but becomes the same in the high-temperature region. Due to the bending effect above T_c we evaluate T_c^{on} and ΔT_c as follows: T_c^{on} is defined as the temperature at which a straight line linearly extrapolated in a narrow temperature region that linearly increases from zero in electrical resistivity near T_c intersects a straight line linearly extrapolated in a temperature region that linearly decreases in electrical resistivity when the temperature in the normal state is lowered to T_c, as shown in Fig. 3. From this definition, the superconducting transition temperature was evaluated as $T_c^{on} = 32.7$ K in the pristine sample and $T_c^{on} = 30.8$ K in the irradiated sample. The T_c^{on} of the pristine sample is almost similar to the reported results [28]. Meanwhile, the transition temperature width ΔT_c was determined from $2 \cdot (T_c^{50\%} - T_c^{10\%})$, where $T_c^{50\%}$ ($T_c^{10\%}$) is the temperature at which the electrical resistivity becomes 50% (10%) of the electrical resistivity magnitude at T_c^{on}. As a result, the width was evaluated as $\Delta T_c = 0.46$ K in the pristine sample and $\Delta T_c = 0.79$ K in the irradiated sample. ΔT_c of the pristine sample is small, indicating that the sample has very few defects such inhomogeneity of the doping of disorder. Compared to the pristine sample, the irradiated sample showed slightly larger ΔT_c, which was not caused by the appearance of any secondary phase because no small peak due to the secondary phases was observed in the XRD experiment results. Instead, this increase in ΔT_c is thought to be due to an increment in the penetration depth by crystallographic distortions [44] because a slight increase in FWHM for the XRD diffraction peaks was observed. However, the crystallographic distortion occurring in the irradiated sample is small because the magnitude of electrical resistivity for the irradiated sample in the high-temperature normal state is almost the same as that of the pristine sample.

As described above, T_c of the irradiated sample is lowered by about 2 K compared to the pristine sample. It is known that the significant decrease in T_c occurs due to the spin flip scattering of the electron pair due to the magnetic defect [45]. The lattice distortion induced by proton irradiation does not induce magnetic defects that cause spin flip scattering of electron pairs, indicating that the lattice distortion is not responsible for the significant decrease in T_c. Another cause for the large decrease in T_c could be the increase of the lattice constants a and b by proton irradiation as discussed in the SAED results above. The increase in the lattice constants a and b is expected to reduce the overlap between the in-plane 3d-bands, resulting in a decrease in the concentration of electrons and to further enhance the localization of the 3d-electron orbit. The former will cause an underdoping effect, resulting in a decrease in T_c, and the latter will cause an increase in electrical resistivity in the normal state just above T_c as in the underdoped Ca 10–3–8 samples. These two behaviors were observed in the irradiated samples, indirectly indicating that a large decrease in T_c caused an increase in the lattice parameters a and b. In addition to this, the disorder at the nanoscale in high-T_c superconductors can also lead to a decrease in T_c due to induction of more isotropic gaps [46], alteration of pairing-symmetry [47], and occurrence of accidental nodes [8,48–50]. However, the nanoscale disorder is independent of the decrease in T_c in the irradiated sample, because as already mentioned in the analysis of SAED patterns, no obvious nanoscale defects were observed in the irradiated sample. However, even if there are nanoscale defects that are not observed with the resolution of SAED, they are not the main cause of the T_c decrease because the amount of these defects is expected to be small.

Electrical resistivity under magnetic field and the higher critical field $B_{c2}(T)$ curves

Fig. 4 (a) − 4 (d) show the temperature dependence of the in-plane electrical resistivity measured with $B//c$ and $B//ab$ for the pristine and irradiated $(Ca_{0.85}La_{0.15})_{10}(Pt_3As_8)(Fe_2As_2)_5$ single crystals, respectively, on a semi-logarithmic scale. For pristine and irradiated samples, the electrical resistivity near T_c shows a typical broadening in both directions of $B//c$ and $B//ab$. The broadening becomes more pronounced
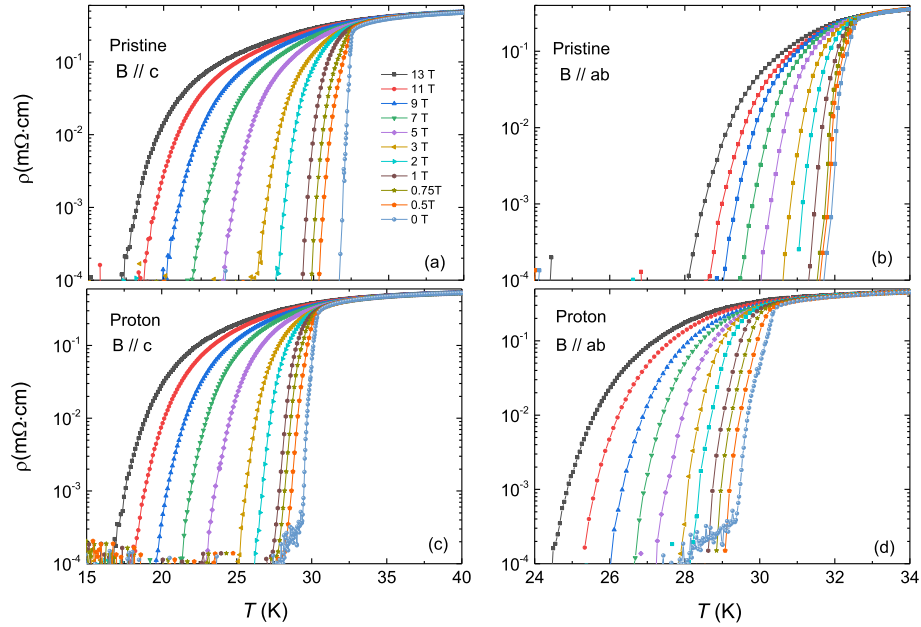

Fig. 3. Temperature dependence of electrical resistivity around superconducting transition temperature for the pristine and irradiated $(Ca_{0.85}La_{0.15})_{10}(Pt_3As_8)(Fe_2As_2)_5$ single crystals. The inset represents the temperature dependence of the electrical resistivity for the two samples over a wider temperature range. The blue dashed lines represent extrapolated lines to determine T_c^{on}. (For interpretation of the references to color in this figure legend, the reader is referred to the web version of this article.)

Fig. 4. Temperature dependence of the in-plane electrical resistivity measured with $B//c$ (a) and $B//ab$ (b) in the pristine $(Ca_{0.85}La_{0.15})_{10}(Pt_3As_8)(Fe_2As_2)_5$ single crystal. Temperature dependence of the in-plane electrical resistivity measured with $B//c$ (c) and $B//ab$ (d) in the irradiated $(Ca_{0.85}La_{0.15})_{10}(Pt_3As_8)(Fe_2As_2)_5$ single crystal.

as the magnetic field increases in both magnetic field directions, especially in $B//c$. This broadening is due to the thermally activated vortex motion occurring in vortex liquid states. On the other hand, the absence of a discontinuous jump to zero resistance in the magnetic field indicates that the first-order vortex liquid-to-solid phase transition does not occur [51]. As shown in the figures, the electrical resistivity scatters at a value less than $\rho \sim 4 \times 10^{-7}$ Ω·cm, which is due to the small electrical resistance of the sample, exceeding the accurately measurable limits.

The temperature dependence of the higher critical fields $B_{c2}^{90\%}$, $B_{c2}^{50\%}$ and $B_{c2}^{10\%}$ in $B//c$ and $B//ab$, determined by applying the 90, 50 and 10% criteria to the electrical resistivity data of pristine and irradiated samples, are shown in Fig. 5 (a) − 5 (d), respectively. $B_{c2}^{90\%}$, $B_{c2}^{50\%}$ and $B_{c2}^{10\%}$

curves show weak upward curvature in the low magnetic field region, which may be due to a weak link of proximity type between superconducting grains or multiband effects. $B_{c2}(0)$, determined by applying the Werthamer-Helfand-Hohenberg (WHH) expression, $B_{c2}(0) = -0.639T_c(dB_{c2}/dT)_{T_c}$, for dirty limit superconductors to each higher critical field in $B > \sim 2$ T, is listed in Table 1. Note that La-doped Ca 10–3–8 is in the dirty limit [31,32]. In all three cases, $B_{c2,c}(0)$, determined by each criterion, was almost similar in pristine and irradiated samples, but $B_{c2,ab}(0)$ showed a significant decrease in irradiated samples. $B_{c2}(0)$ obtained by the 90% criterion is unusually large, probably because $B_{c2}(0)$ cannot be accurately obtained by the round effect of electrical resistivity near T_c. The in-plane Ginzburg-Landau coherence
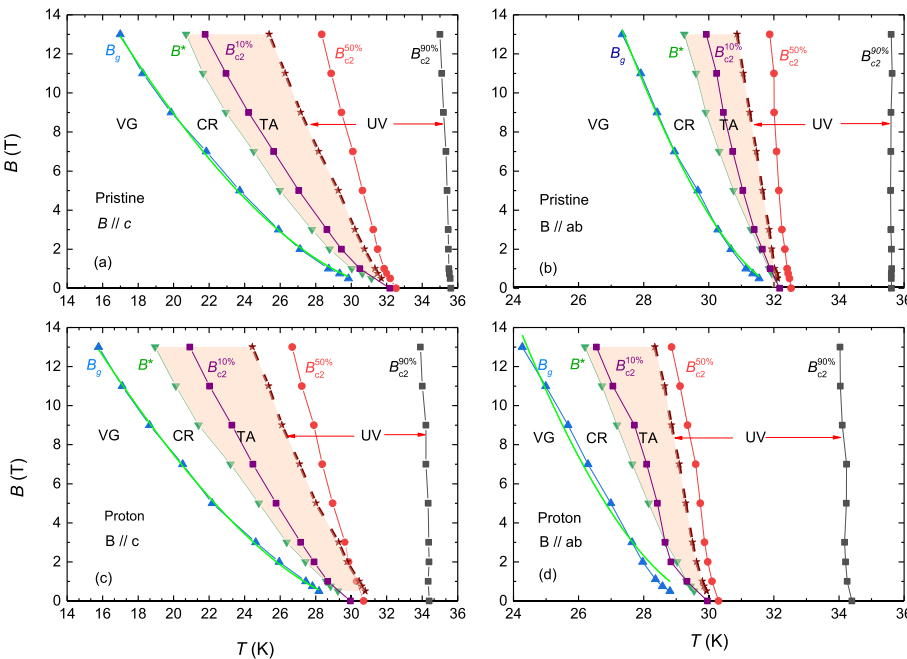

Fig. 5. Temperature dependence of the higher critical fields $B_{c2}^{90\%}$, $B_{c2}^{50\%}$ and $B_{c2}^{10\%}$ determined by the 90, 50 and 10% criteria in the electrical resistivity data of $(Ca_{0.85}La_{0.15})_{10}(Pt_3As_8)(Fe_2As_2)_5$ single crystals: (a) for $B//c$ and (b) for $B//ab$ in the pristine sample, and (c) for $B//c$ and (d) for $B//ab$ in the irradiated sample. The figure also shows the vortex glass magnetic field B_g and the magnetic field B^* that separates CR and TA in the vortex liquid. Here, VG, CR, TA and UV denote the vortex glass, critical, thermally activated flux motion and unpinned vortex regions, respectively. The wine-colored dashed line represents the separation between the thermally activated flux flow region and the unpinned vortex liquid region. The green-colored solid line represents the glass line fitted by $B_g(T) = B_0(1 - T/T_c)^m$. (For interpretation of the references to color in this figure legend, the reader is referred to the web version of this article.)

Table 1

The higher critical fields B_{c2} and coherence lengths ξ evaluated by the 90, 50 and 10% criteria in pristine and irradiated samples.

	Pristine sample				Irradiated sample			
	$B_{c2,c}(0)$	$B_{c2,ab}(0)$	$\xi_{ab}(0)$	$\xi_c(0)$	$B_{c2,c}(0)$	$B_{c2,ab}(0)$	$\xi_{ab}(0)$	$\xi_c(0)$
10%	32.5 T	154.1 T	31.8 Å	6.7 Å	33.3 T	94.0 T	31.5 Å	11.1 Å
50%	77.0 T	631.1 T	20.7 Å	2.5 Å	74.6 T	197.6 T	21.0 Å	7.9 Å
90%	499.5 T	3715.7 T	8.1 Å	1.1 Å	469.4 T	818.5 T	8.4 Å	4.8 Å

length $\xi_{ab}(0)$, evaluated from the equation $\xi_{ab}(0) = \left(\frac{\phi_0}{2\pi B_{c2,c}(0)}\right)^{1/2}$, and the out-of-plane Ginzburg-Landau coherence length $\xi_c(0)$, evaluated from the determined value of $\xi_{ab}(0)$ and the equation $\xi_c(0) = \frac{\phi_0}{2\pi B_{c2,ab}(0)\xi_{ab}(0)}$, are listed in Table. 1. Here, ϕ_0 is the magnetic flux quantum, 2.07×10^{-15} Wb. The coherence lengths $\xi(0)$ in the two directions evaluated by the 90% criterion are quite different from those evaluated by the other criteria. The reasons have already been discussed above. The coherence lengths determined by other two criteria also differ, but the difference is not significant. An important result for both criteria is that the in-plane coherence length $\xi_{ab}(0)$ in the pristine sample is longer than $\xi_c(0)$ in the direction perpendicular to the plane, resulting in anisotropy $\gamma_\xi \sim$ 5–8. On the other hand, in the case of the irradiated sample, the in-plane coherence length $\xi_{ab}(0)$ is almost similar to that of the pristine sample, but the coherence length $\xi_c(0)$ perpendicular to the plane increases significantly, resulting in anisotropy $\gamma_\xi \sim$ 3. The coherence length $\xi_c(0)$ evaluated by the previously reported superconducting fluctuation method is $\xi_c(0) = 5.8$ Å for the pristine sample and 9.9 Å for the irradiated sample [52], which is more similar to $\xi_c(0)$ obtained with the 10% criterion. Lattice distortion and point defects caused by proton irradiation induce a decrease in the mean free path of electrons, leading to a shortening of the coherence length. As discussed above, these results are notconsistent in the irradiated sample. Therefore, the reduction of anisotropy in the irradiated sample is not simple, and we intend to discuss this point.

When La is optimally doped to the parent Ca 10–3–8, lattice constants a and b are almost invariant and c increases by 0.34% [40,53]. On the other hand, when Pt is optimally doped, the lattice constants a, b, and c increase by 0.10–0.24% [53,54]. This increase in these samples was caused by the doping of La/Pt with a large ion radius, which would cause a change in the distance between Fe-As ions and the angle between As-Fe-As ions in the conducting Fe_2As_2 layer. The distance between Fe-As ions and angle between As-Fe-As ions in the Fe_2As_2 layer causes a change in the overlap between the Fe-3d wavefunctions and the hybridization between the Fe-3d wavefunctions and the As-4p wavefunctions. In the irradiated sample, the lattice constant c remains unchanged, but a and b increase by 0.42–0.6%. If we consider this small increase in lattice constant caused by proton irradiation as a change in lattice constant in Pt-doped Ca 10–3–8 as an example, this increase corresponds to the difference in lattice constant between parent Ca 10–3–8 and Pt-overdoped Ca 10–3–8. This indicates that this small change in the lattice constant can cause very large changes in the physical properties of material. The irradiated sample has an increased interatomic distance without ion doping. This increased distance obviously further reduces the overlap between the Fe-3d wavefunctions in the Fe_2As_2 layer, which causes further localization of the 3d wavefunctions. Unlike the pristine sample, the irradiated sample shows a weak increase in electrical resistivity below 70 K due to this localization. A similar increase in electrical resistivity was observed for Pt-underdoped Ca 10–3–8 [21]. These localized 3d-electrons should cause greater anisotropy, but as discussed earlier, the irradiated samples show less anisotropy. Therefore, the decrease in anisotropy of the irradiated sample cannot be explained by the overlap of the 3d-wave functions.

In the band structure of a substance having a localized state, for example, heavy fermion [55] band, hybridization reduces the

localization of the band, which leads to the three-dimensionality of the band. Based on this, the small anisotropy in the irradiated sample can be attributed to the change in the hybridization magnitude between the Fe-3d and As-4p wavefunctions. In pristine and irradiated samples, the lattice constant c is constant, but the angle γ in the unit cell is changed by $\sim 1°$ as discussed previously. This change in angle γ can change the distance between Fe-As and the angle between As-Fe-As, resulting in a change in this hybridization magnitude. In this sense, we propose that the decrease in anisotropy in the irradiated samples is caused by changes in the electronic structure determined by the hybridization of the Fe-3d and As-4p wavefunctions. Accurate band calculation is required to make this clear.

Thermally activated flux motion in the vortex liquid state

The temperature dependence of the measured in-plane electrical resistivity for the pristine and irradiated samples shown in Fig. 4 (a) − 4 (d) is understood as thermally activated flux motion (TAFM) in the vortex liquid state as described above. According to TAFM theory, the electrical resistivity [56,57] is given by

$$\rho(T) = (2\rho_c U(T,B)/T)\exp(-U(T,B)/T) \quad (1)$$

where $U(T,B) = J_{c0}BVL$ is the thermal activation energy and $\rho_c = \nu_0 LB/J_{c0}$. Here, ν_0, L, J, J_{c0} and V are the attempt frequency for a flux bundle hopping, hopping distance, applied current density, critical current density in the absence of flux creep, and bundle volume, respectively. In cuprate and iron-based superconductors, the prefactor $2\rho_c U/T$ is usually assumed to be a constant ρ_{0f} and the thermal activation energy is assumed to be in the form of $U(T,B) = U_0(B)(1-t)$, where $t = T/T_c$ and $U_0(B)$ is the zero-temperature activation energy. Taking the natural logarithm of Eq. (1) gives $\ln\rho(T,B) = \ln\rho_0(B) - U_0(B)/T$, where $\ln\rho_0(B) = \ln\rho_{0f} + U_0(B)/T_c$. This analysis shows that the zero temperature activation energy is given by the equation $-\partial\ln\rho/\partial(1/T) = U_0(B)$. The so-called Arrhenius plot with the relation $\ln\rho(1/T,B)$ can easily determine $U_0(B)$ with the corresponding slope in the low resistivity range. However, the assumption of $U(T,B) = U_0(B)(1-t)$ and/or ρ_{0f} = constant is not valid for both pristine and irradiated samples because the Arrhenius plot shown in Fig. 9 (a) – (d) does not exhibit a linear dependence but rather a rounded curvature.

Zhang et al. [58,59] suggested a temperature-dependent prefactor in Eq. (1) with nonlinear $U(T,B) = U_0(B)(1-t)^q$. Using the nonlinear activation energy, the logarithm of Eq. (1) is given by

$$D(T) \equiv \ln\rho(T) = \ln(2\rho_c U_0(B)) + q\ln(1-t) - \ln T - U_0(B)(1-t)^q/T, \quad (2)$$

and then the derivative by $1/T$ for Eq. (2) is expressed as

$$U_a(T) \equiv -\partial\ln\rho/\partial(1/T) = [U_0(B)(1-t)^q - T][1 + qt/(1-t)], \quad (3)$$

where q has a value in the range from 0.5 to 2 and $t = T/T_c$. In our study, the temperature-dependent pre-factor is simply considered by the temperature nonlinear activation energy and constant ρ_c. $U_a(T)$ calculated from the measured data in the directions of $B//c$ and $B//ab$ at $B = 13$ T agrees well with the red line fitted by Eq. (3) over a limited temperature range for the pristine and irradiated samples as shown in Fig. 6 (a-1) − 6 (a-4). This best fit for different magnetic fields is shown by red lines in Fig. 7 (a) − 7 (d). $T_c = 32.3$ K and $q = 1.52$ for the pristine sample and T_c
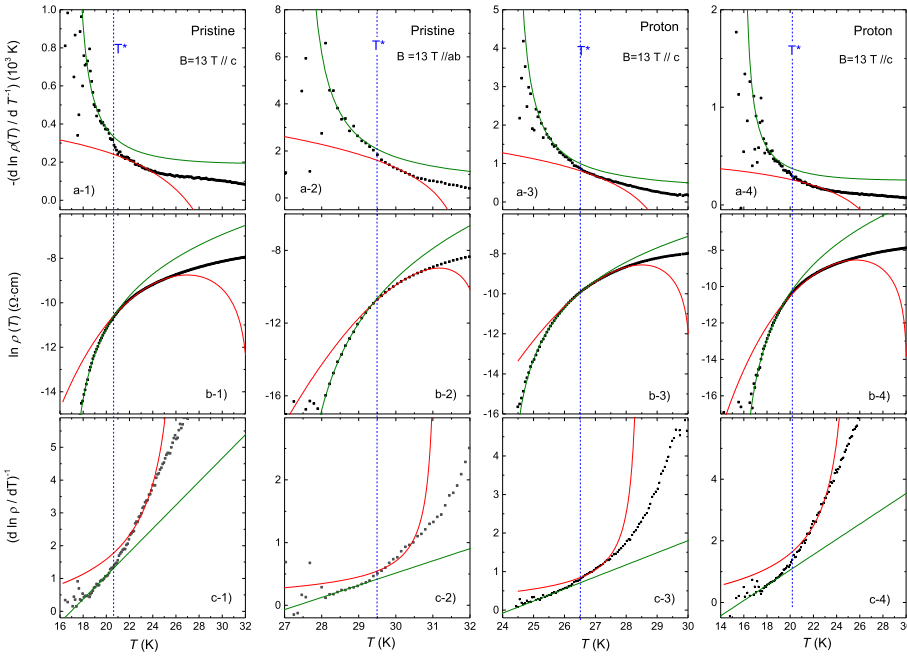
Fig. 6. Derivatives from in-plane electrical resistivity measured on the pristine and irradiated $(Ca_{0.85}La_{0.15})_{10}(Pt_3As_8)(Fe_2As_2)_5$ single crystals at $B = 13$ T. (a-1) − (a-4): derivatives $U_a = (dln\rho(T))/(dT^{-1})$ in $B//c$ and $B//ab$ for each sample, respectively. The red line represents the best fit using Eq. (3) and the green line is the best fit using expression $\rho(T) = \rho_n\left[\exp\left(U_{eff}/k_BT\right)\right]^s$ with $U_{eff} = k_BT(T_c - T)/(T_c - T_g)$. (b-1) − (b-4): derivatives $D = \ln\rho(T)$ in $B//c$ and $B//ab$ for each sample, respectively. The red line represents the best fit using Eq. (2) and the green line is the best fit using expression $\rho(T) = \rho_n\left[\exp\left(U_{eff}/k_BT\right)\right]^s$ with $U_{eff} = k_BT(T_c - T)/(T_c - T_g)$. (c-1) − (c-4): derivatives $R = (dln\rho(T)/dT)^{-1}$ in $B//c$ and $B//ab$ for each sample, respectively. The red line is derived using the parameters obtained from the fitting for the TAFM model indicated by the red line in the graphs of (a-1) − (a-4) and the green line represents the best fit using Eq. (4). (For interpretation of the references to color in this figure legend, the reader is referred to the web version of this article.)
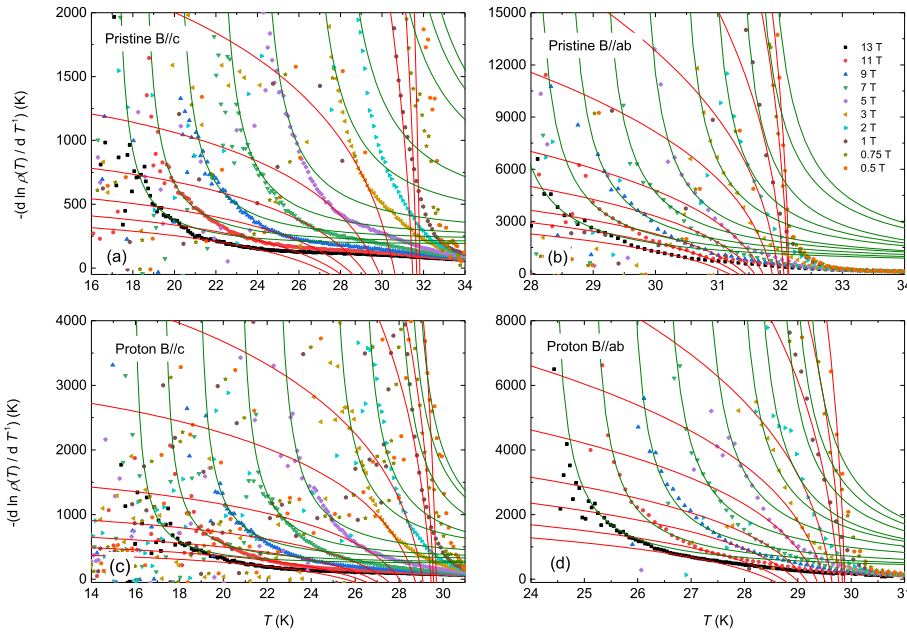

Fig. 7. (a) to (d) represent the temperature dependence of $U_a = (dln\rho(T))/(dT^{-1})$ for various magnetic fields with $B//c$ and $B//ab$ in pristine and irradiated $(Ca_{0.85}La_{0.15})_{10}(Pt_3As_8)(Fe_2As_2)_5$ single crystals, respectively. The red line represents the best fit using Eq. (3) and the green line represents the best fit using expression $\rho(T) = \rho_n\left[\exp\left(U_{eff}/k_BT\right)\right]^s$ with $U_{eff} = k_BT(T_c - T)/(T_c - T_g)$. (For interpretation of the references to color in this figure legend, the reader is referred to the web version of this article.)

$= 30.1$ K and $q = 1.52$ for the irradiated sample were determined from the fittings. The exponent q will be discussed later. Also, the zero-temperature activation energy $U_0(B)$ determined by the fittings is shown in Fig. 8. $U_0(B)$ for $B//c$ varies almost linearly on log scale, but for $B//ab$ it deviates from the linear change and curves downwards, which is discussed later. The best fitting using Eq. (2) with the values of T_c, q, and U_0 obtained from the $U_a(T)$ fitting at $B = 13$ T performed just above is shown as a red line in Fig. 6 (b-1) − 6 (b-4). In the above two fittings, the temperature range consistent with the experimental results is almost the same. The fitting results using Eq. (2) for different magnetic fields are drawn with red lines in Fig. 9 (a) − 9 (d). $\rho_c(B)$ determined in this fitting is shown in the inset of Fig. 8. $\rho_c(B)$ increases rapidly in the low magnetic field region and then becomes almost saturated above $B = 1$ T. This behavior of $\rho_c(B) = \nu_0 LB/J_{c0}$ may be mainly due to the magnetic

field dependence of J_{c0}. Note that J_{c0} in the prototype iron-based superconductor shows a small change at a low magnetic field and then decreases rapidly as the magnetic field increases [60,61].

As shown in Fig. 6 (a-1) − 6 (a-4), $U_a(T)$ calculated from the measured electrical resistivity deviates from the red line calculated by TAFM below T^* and scatters greatly in the lower temperature region. This value scattering is due to measurement error due to the sample's electrical resistance being very close to zero and exceeding the measurement limit, indicating that both samples have a secondary phase transition from the vortex liquid phase to the vortex glass phase. From this point of view, the gradual deviation of the experimental value $U_a(T)$ from the data calculated from the TAFM model (red line) toward larger values below T^* is due to the development of vortex glass that appears gradually as the temperature decreases in the vortex liquid state. The
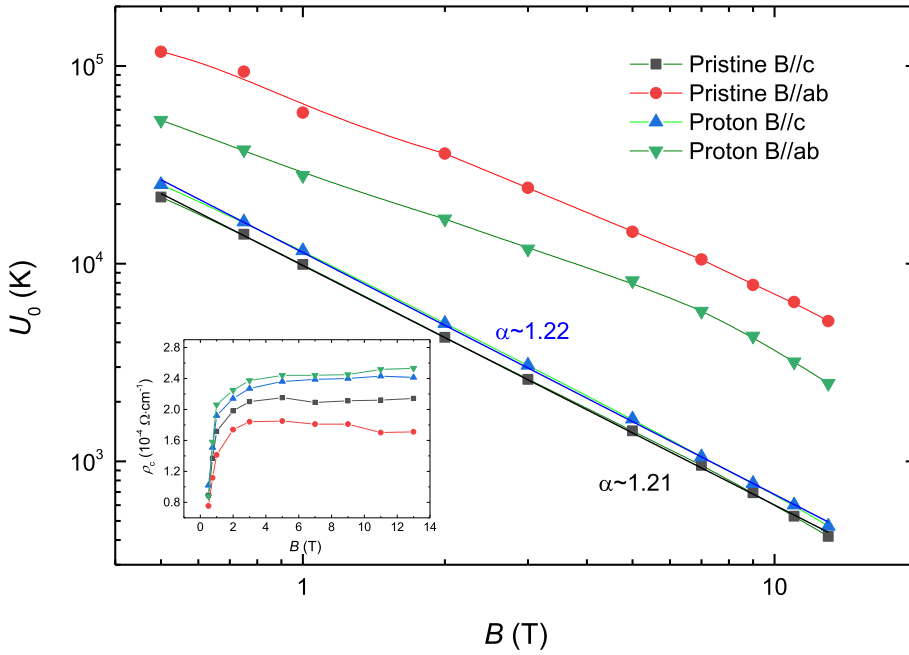
Fig. 8. Magnetic field dependence of thermal activation energy $U_0(B)$ in magnetic flux motion for $B//c$ and $B//ab$ in the pristine and irradiated $(Ca_{0.85}La_{0.15})_{10}(Pt_3As_8)(Fe_2As_2)_5$ single crystals. The black and blue lines represent the linear fitting result of $U_0(B)$ obtained from pristine samples, and the red and green lines are visually drawn to see the trend of $U_0(B)$. The inset shows the magnetic field dependence of the parameter $\rho_c(B)$ included in Eq. (2) for the pristine and irradiated single crystals in $B//c$ and $B//ab$. (For interpretation of the references to color in this figure legend, the reader is referred to the web version of this article.)
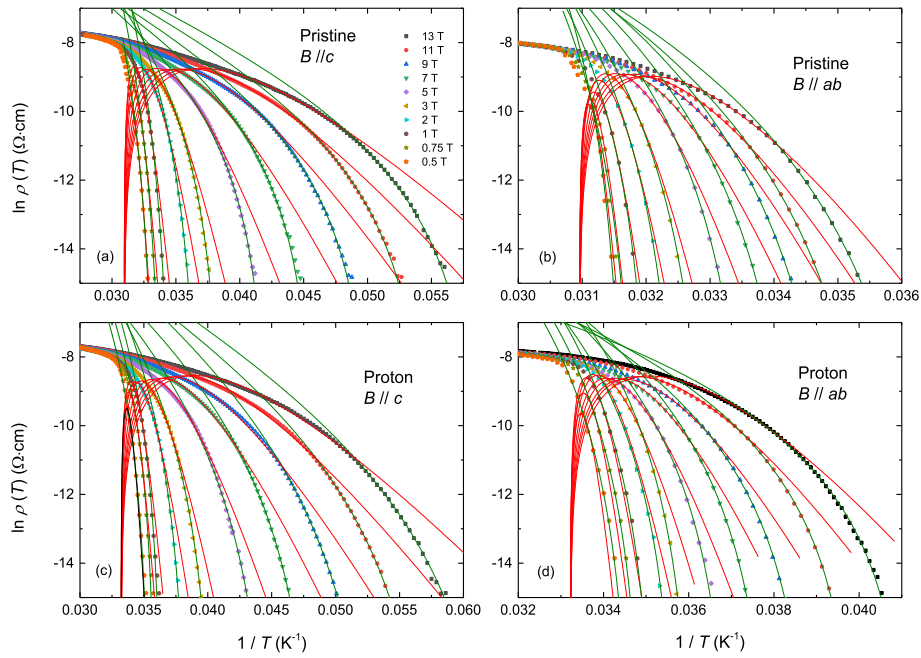

Fig. 9. (a) to (d) represent $D = \ln\rho(T)$ vs. $1/T$ plots for various magnetic fields with $B//c$ and $B//ab$ in the pristine and irradiated $(Ca_{0.85}La_{0.15})_{10}(Pt_3As_8)(Fe_2As_2)_5$ single crystals, respectively. The red line represents the best fit using Eq. (2) and the green line is the best fit using expression $\rho(T) = \rho_n\left[\exp\left(U_{eff}/k_BT\right)\right]^s$ with $U_{eff} = k_BT(T_c-T)/(T_c-T_g)$. (For interpretation of the references to color in this figure legend, the reader is referred to the web version of this article.)

development of vortex glass in this temperature region effectively increases the activation energy against vortex depinning, and this region is called the critical region. According to the vortex glass theory [62], which quantitatively explains the temperature dependence of the electrical resistivity in this critical region, the electrical resistivity satisfies $\rho(T) \sim |T - T_g|^{\nu(z+2-d)}$ and is completely suppressed at T_g, where d is the dimensionality of the sample ($d = 3$ in both samples), ν is a static index for the vortex-glass correlation length, and z is a dynamic index for the correlation time. The derivative of the logarithmic electrical resistivity by temperature in this region shows a linear temperature dependence, that is,

$$R(T) \equiv \left(\frac{d\ln\rho(T)}{dT}\right)^{-1} = \frac{1}{s}\left(T - T_g\right) \qquad (4)$$

where $s = \nu(z + 2 - d)$ is the reciprocal of the slope of Eq. (4). $R(T)$ calculated from the electrical resistivity measured in the $B//c$ and $B//ab$ directions at $B = 13$ T is shown in Fig. 6 (c-1) – 6 (c-4) for the pristine sample and the irradiated sample, respectively. As can be seen from the figures, according to the vortex glass theory, a linear change in $R(T)$ is observed in the temperature range below T^*, and the linear fit in this region is shown as green lines. $R(T)$ in different magnetic fields is shown in Fig. 10 (a) – 10 (d), and the linear change is observed in all magnetic
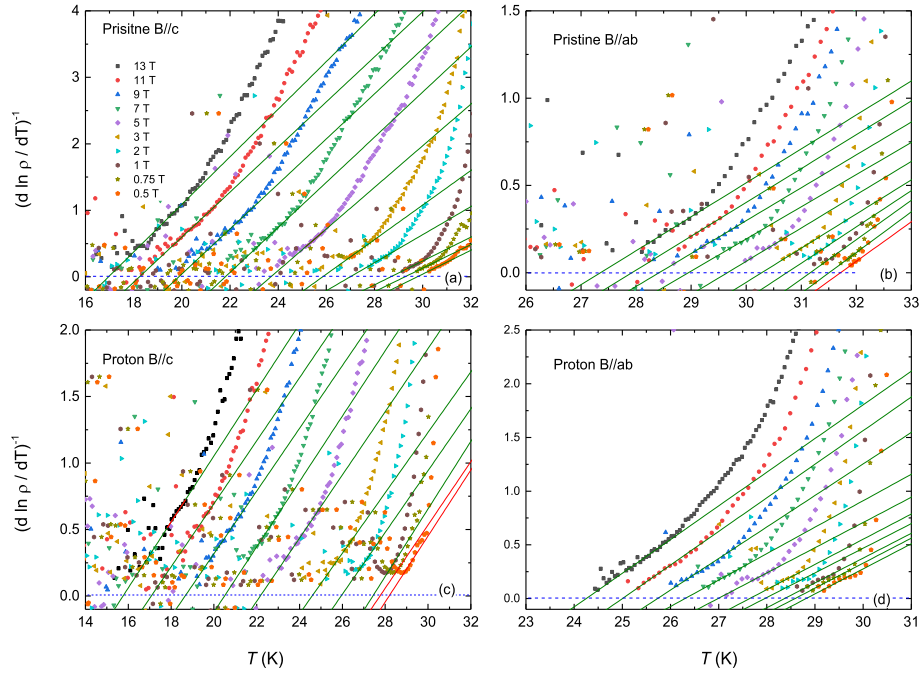
Fig. 10. The temperature dependence of $R = (\mathrm{d}\ln\rho(T)/\mathrm{d}T)^{-1}$ at different magnetic fields in $B//c$ and $B//ab$ for (a)-(b) pristine and (c)-(d) irradiated $(Ca_{0.85}La_{0.15})_{10}(Pt_3As_8)(Fe_2As_2)_5$ single crystals. The green line represents the best fitting using Eq. (4). (For interpretation of the references to color in this figure legend, the reader is referred to the web version of this article.)

fields. The best fit obtained using Eq. (4) is also shown as green lines in the figures. These fittings agree well with the experimental results up to T^*. $R(T)$ calculated from the TAFM model discussed above is drawn with red lines in Fig. 6 (c-1) – 6 (c-4). It showed good agreement with the experiment in the limited temperature range above T^*. Therefore, T^* becomes the temperature that divides the TAFM temperature region and the critical temperature region. From the fitting using Eq. (4) shown in Fig. 10 (a) – 10 (d), the vortex glass temperature T_g and critical exponent s were determined. The magnetic field dependence of T_g, which is termed $B_g(T)$, and s are shown in Fig. 5 (a) – (d) and 11 (a) – (d), respectively. s will be discussed later.

According to Liu et al. [63], the thermal activation energy in the

critical region is given by $U_{\mathrm{eff}} = k_B T(T_c - T)/(T_c - T_g)$, and the temperature dependence of the electrical resistivity with this activation energy is given by $\rho(T) = \rho_n \left[\exp\left(U_{\mathrm{eff}}/k_B T\right)\right]^s$, which is consistent with the Eq. (4) obtained by the vortex-glass theory [62,63]. When the electrical resistivity $\rho(T)$ is plotted on the new temperature scale $(T - T_g)/(T_c - T_g)$ in the critical region, according to Eq. (4), $\rho(T)$ is scaled to one in all magnetic fields if s is constant with respect to the magnetic field change. Fig. 12 (a) – 12 (d) show the electrical resistivity in two magnetic field direction for the pristine and irradiated samples on a temperature scale of $(T - T_g)/(T_c - T_g)$, respectively. Here, T_c and T_g were the values determined from the fittings discussed above. $\rho(T)$
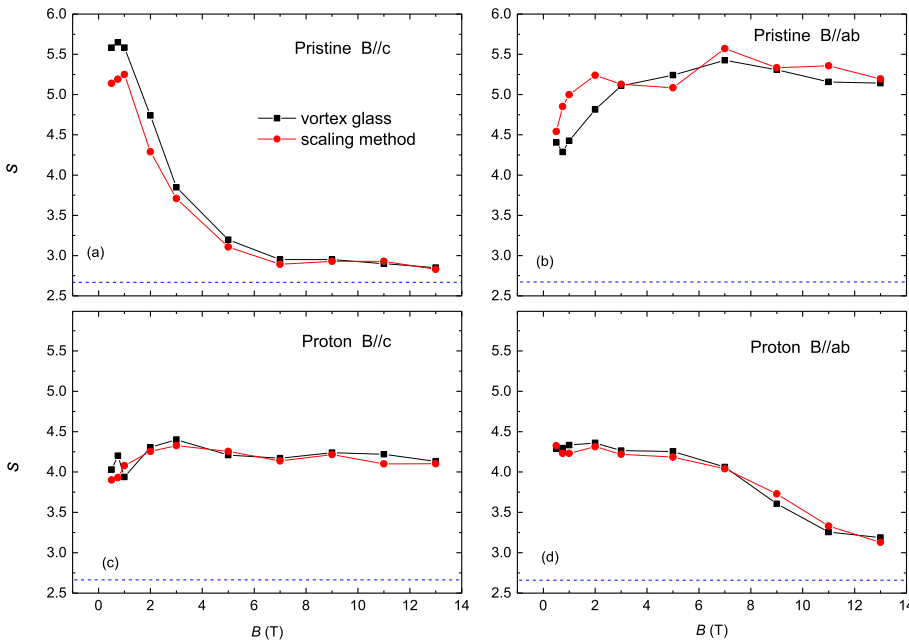

Fig. 11. (a) to (d) show the magnetic field dependence of determined fitting parameter s for the pristine and irradiated $(Ca_{0.85}La_{0.15})_{10}(Pt_3As_8)(Fe_2As_2)_5$ single crystals in $B//c$ and $B//ab$, respectively. The solid square in black represents s obtained by fitting the experimental data using Eq. (4) for the vortex glass model in different magnetic fields, and the red solid circle represents s determined from the dependence of the new temperature scale $(T - T_g)/(T_c - T_g)$ of the electrical resistivity in the critical region. The blue dashed line represents $s = 2.7$, which is a three-dimensional vortex glass limit. (For interpretation of the references to color in this figure legend, the reader is referred to the web version of this article.)

scales well with $(T - T_g)/(T_c - T_g)$ in $B//ab$ for the pristine sample and in $B//c$ for the irradiated sample, indicating that s has little dependence on the magnetic field. The s-field dependence obtained from the slope of the graph in the critical region is plotted as red circles in Fig. 11 (a) – 11 (d). As shown in the figures, the two determined s yield consistent results. $U_a(T)$ and $D(T)$ calculated from $\rho(T) = \rho_n \left[\exp(U_{\text{eff}}/k_B T) \right]^s$ along with the values obtained for s, T_c, and T_g in each magnetic field are shown by green lines in Fig. 7 (a) – 7 (d) and Fig. 9 (a) – 9 (d), respectively. These lines agree well with the experimental results in the temperature range below T^*.

Next, let's discuss the magnetic field dependence of the zero-temperature activation energy $U_0(B)$. As shown in Fig. 8, $U_0(B)$ for the pristine and irradiated samples in $B//c$ decreases linearly with increasing magnetic field on a log–log scale in the entire measured magnetic field region, implying a decrease in the form of $U_0(B) \sim B^{-\alpha}$. In both samples, the exponent is almost the same as $\alpha = 1.21$–1.22. Table 2 lists the zero activation energies $U_0(1T)$ at $B = 1$ T and exponents for $B//c$-axis previously reported in iron-based superconductors with similar T_c and $U_0(B) \sim B^{-\alpha}$ form. $U_0(1T)$ varies from 3000 to 17000 K. As for the magnetic field dependence of $U_0(B)$, as in our results, some samples are expressed with one exponent in the entire measured magnetic fields, and some samples are expressed with two exponents. The exponent varies from ~ 0.1 to ~ 1. The vortex is pinned by the normal state component formed in the sample. These normal state components include point defects, twins, and normal state region caused by short coherence. First, consider vortex pinning for the $B//c$-axis. Twins are not considered pinning centers in our sample because they were not observed in SAED. Point defects consist of impurities and vacancies. These point defects are the pinning centers in the pristine and irradiated samples. The density of point defects increases in the irradiated sample. The coherence length in the direction perpendicular to the c-axis is about $20 \sim 32$ Å, which is about $2.5 \sim 4$ times larger than the lattice constants a and b. Such a large coherence length does not create a normal state region with zero Cooper pair in the ab-plane. Therefore, the normal state component that pinning the vortex in the prisitne sample is atomic point defects such as impurity atoms and vacancies, and the normal state component in the irradiated sample is point defects created

Table 2
Zero-temperature activation energies $U_0(1$ T$)$ at $B = 1$ T and exponents α previously reported in iron-based superconductors.

Samples	T_c	U_0 (1 T)	Exponents α
Pristine sample (this study)	32.7 K	~ 9900 K	1.21 (0 < B < 13 T)
Irradiated sample (this study)	30.8 K	~ 11000 K	1.22 (0 < B < 13 T)
$(Ca_{0.85}La_{0.15})_{10}(Pt_3As_8)(Fe_2As_2)_5$ [37]	32.6 K	~ 11000 K	1.11 (0 < B < 5 T)
$Ba_{0.72}K_{0.28}Fe_2As_2$ [74]	~ 32.5 K	~ 5000 K	0.13 (0 < B < 13 T)
$Ca_{0.8}La_{0.2}Fe_{0.98}Co_{0.02}As_2$ [75]	~ 38 K	~ 9000 K	0.34 (0 < B < 2 T) / 0.62 (2 < B < 9 T)
$Ca_{0.77}La_{0.18}Fe_{0.90}As_2$ [76]	42.6 K	~ 3000 K	0.13 (0 < B < 1 T) / 0.56 (1 < B < 9 T)
$SmFeAsO_{0.85}$ [77]	~ 50 K	~ 13000 K	0.35 (0 < B < 3 T) / 0.88 (3 < B < 9 T)
$SmFeAsO_{0.8}F_{0.2}$ [78]	~ 52 K	~ 17000 K	~ 1 (0.5 < B < 9 T)
$Tl_{0.58}Rb_{0.42}Fe_{1.72}Se_2$ [79]	33.5 K	~ 5000 K	0.22 (2 < B < 14 T)

by proton irradiation in addition to these atomic point defects. U_0 decreases in the form of $U_0(B) \sim B^{-\alpha}$ as the magnetic field increases. This cannot be understood with the elastic collective creep theory [56], in which an increase in U_0 is predicted at high magnetic fields [64,65]. The vortex pinning due to random point defects follows the plastic creep theory [66–68]. According to this theory, the entanglement of vortex lines weakly pinned to point defects in the vortex liquid exhibits zero activation energies in the form $U_0(B) \sim B^{-\alpha}$ with $\alpha = 0.5$. Due to the relative motion that occurs between the entangled vortex lines, the vortex lines will be cut off or recombined and eventually change to a new state of vortex motion. This new motion allows the exponent α to change around 0.5. As an example, untwinned YBCO showed $\alpha \sim 0.7$ by vortex entanglement in weakly pinned vortex liquid [51]. On the other hand, the strong plastic pinning shows a stronger magnetic field dependence of $U_0(B)$ with a larger exponent α [51]. Here, the strong pinning is due to further plasticity of the vortex liquid. The exponent α of the pristine sample is larger than α in YBCO, indicating that further
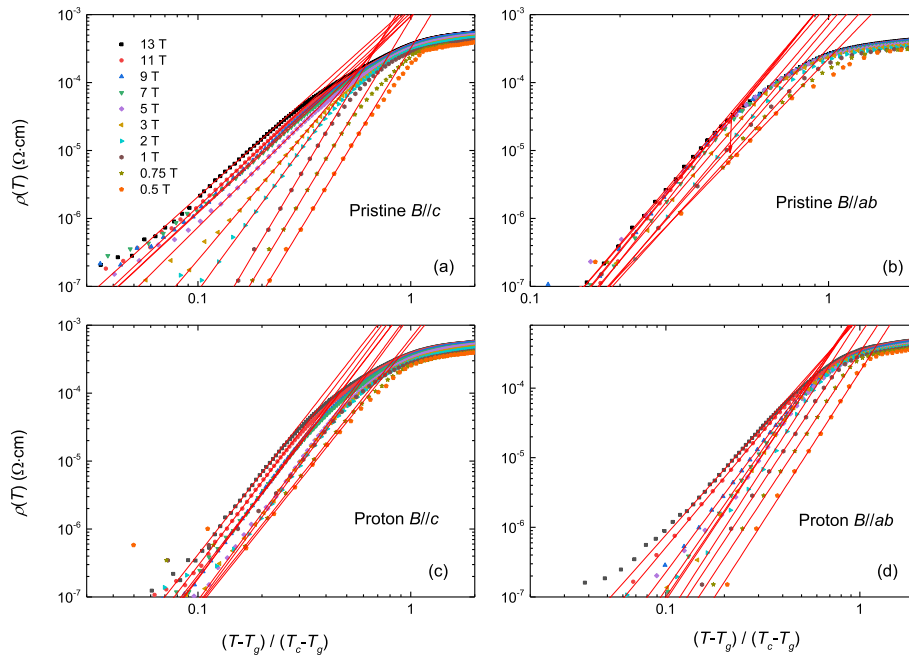

Fig. 12. (a) to (d) show the dependence of the electrical resistivity on the new temperature scale $(T - T_g)/(T_c - T_g)$ for the pristine and irradiated $(Ca_{0.85}La_{0.15})_{10}(Pt_3As_8)(Fe_2As_2)_5$ single crystals in $B//c$ and $B//ab$, respectively. The red line represents the linear best fitting in the critical region. (For interpretation of the references to color in this figure legend, the reader is referred to the web version of this article.)

plasticization of the vortex liquid caused the vortex to pin strongly to point defects, as inferred by the plastic creep theory mentioned above [66–68]. The magnetic field dependence of U_0 in the irradiated sample is similar to that in the pristine sample, indicating that pinning in the irradiated sample is the same as that of the pristine sample. However, the zero-temperature activation energy magnitude of the irradiated sample increases by about 15% compared to that of the pristine sample in the entire magnetic field region. This increase is due to an increase in point defects created by proton irradiation. This pinning energy increase by irradiation is predicted to cause an increase in the critical current density J_c. As shown in Table 2, the magnitude of the exponent α varies from sample to sample, which is understood as the degree of plasticity of the material in terms of the plastic creep model applied here. Weakly pinned vortex lines to point defects are predicted to occur at lower magnetic fields, which requires further study.

Next, consider vortex pinning for the $B//ab$-axis. Both the pristine and irradiated samples in $B//ab$ show significantly larger zero-temperature activation energy $U_0(B)$ in the entire measured magnetic field region compared to those in $B//c$. In addition to this, $U_0(B)$ of the pristine sample was significantly larger than that of the irradiated sample, which is the opposite of the result on the $B//c$-axis. The coherence length ξ_c of the two samples discussed above is shorter than or approximately similar to the distance between the superconducting Fe_2As_2 layers ($d = 10.4$ Å). In particular, it is much shorter in the pristine sample. According to the definition of the coherence length, its short length results in a normal state region with zero Cooper pairs. The coherence length obtained above is the value at $T = 0$, whereas the behavior of vortex pinning discussed in this study was observed at a high temperature below T_c. Considering this, the normal-like state referred to herein means a relatively weak superconducting state compared to the strong superconducting state on the Fe_2As_2 layers. The normal-like state region forms a long plate shape parallel to the ab-plane. The normal-like state region formed by the short ξ_c serves as the vortex pinning center in $B//ab$. Of course, as in $B//c$, pinning by defects such as impurity atoms, vacancies, and point defects is also included. According to the theory of normal-like state pinning due to short coherence length discussed in the introduction [14,69], the vortex pinning by long normal-like state is not only stronger than atomic or point defects, but also stronger at shorter coherence lengths. The short coherence length in both samples, although this increased to the distance between the Fe_2As_2 planes in the irradiated sample, produces a normal-like state region. The pinning energy due to the normal-like state region is expected to be greater than that due to point defects. This pinning caused the magnetic field dependence to deviate from the $U_0(B) \sim B^{-\alpha}$ form, which is due to plastic vortex pinning by point defects, as shown in Fig. 8. The smaller $U_0(B)$ in the irradiated sample than in the pristine sample is well explained from the c-axis coherence length ξ_c elongated by proton irradiation. According to this pinning mechanism in $B//ab$, we can infer that the coherence length increases in the high magnetic field from the bending of $U_0(B)$ in the high magnetic field. A detailed study of this is needed. Differences in vortex pinning in both directions may also be affected by changes in superfluid density [70].

As discussed above, $U_0(T)$ in the vortex liquid depends on the temperature power law, i.e. $U(T,B) = U_0(B)(1-t)^q$. The exponent q was determined to be 1.52 for both magnetic field directions in the pristine and irradiated samples. Note that $q = 1.5$ is observed in 3-dimensional high-T_c superconductor and $q = 2$ is observed in 2-dimensional high-T_c superconductor. The pristine sample showed anisotropy $\gamma_\xi \sim 5$–8 and the irradiated sample showed $\gamma_\xi \sim 3$, but both samples formed 3D vortex without forming 2D-disk type vortex in vortex liquid state.

The magnetic field dependence of s representing the vortex glass dimensions determined in the $B//c$ and $B//ab$ for pristine and irradiated samples is shown in Fig. 11 (a) − 11 (d), respectively. In both magnetic field directions for both samples, s is greater than 2.7 in the entire measured magnetic field region, indicating that a three-dimensional

vortex glass is formed. The s for $B//c$ of the pristine sample and $B//ab$ of the irradiated sample show strong magnetic field dependence, whereas the s for $B//ab$ of the pristine sample and $B//c$ of the irradiated sample are almost constant with respect to the change in the magnetic field. The complex magnetic field dependence of s suggests that vortex glass can follow theories such as window glass and kinetic transitions [71] rather than the traditional vortex glass theory with power law scaling methods [62]. Further research is needed on this.

$B(T)$ phase diagrams for pristine and irradiated samples in $B//c$ and $B//ab$ are shown in Fig. 5 (a) − 5 (d), respectively. Each $B(T)$ phase diagram is largely divided into four different regions. The vortex glass-to-vortex liquid transition occurs at $B_g(T)$, which divides the vortex glass region and vortex liquid region. This vortex glass line is well represented by $B_g(T) = B_0(1 - T/T_c)^m$ where B_0 is the zero-temperature vortex glass field and m is the exponent. The best fitting with this equation is shown as green lines in Fig. 5 (a) − 5(d). The parameters determined in the pristine sample are $B_0 = 45.2$, $m = 1.7$ for $B//c$ and $B_0 = 279.52$, $m = 1.6$ for $B//ab$. On the other hand, the parameters determined in the irradiated sample are $B_0 = 40.7$, $m = 1.6$ for $B//c$, and $B_0 = 234.4$, $m = 1.7$ for $B//ab$. The evaluated m is similar to the values determined for cuprate and iron-based superconductors [63,72,73]. The vortex liquid region is divided by $B^*(T)$ into a critical region in contact with T_g and a thermally activated flux flow region. The thermally activated flux flow region and the unpinned vortex liquid region were separated by a wine-colored dashed line. This separation line is obtained from the higher temperature that deviates between the results using the TAFM model and the experimental data.

Conclusion

We grew optimally doped $(Ca_{0.85}La_{0.15})_{10}(Pt_3As_8)(Fe_2As_2)_5$ single crystals and measured in-plane electrical resistivity with $B//c$ and $B//ab$ to study the difference between vortex pinning in pristine and irradiated samples. As a result of analyzing the crystal structure of the two samples by the selected area electron diffraction (SAED) method using TEM, the diffraction patterns of both samples were not explained by the known triclinic structure but were explained by the monoclinic crystal structure. In addition, in the lattice structure, the lattice constants of a and b in the irradiated sample increased compared to that of the pristine sample, but the lattice constant of c did not change. The increase in the lattice constant caused a change in their electronic structure due to the change in the overlap effect between Fe-3d wavefunctions and the hybridization effect of Fe-3d wavefunction and As-4p. This change showed a significant difference in superconducting transition temperature and anisotropy between the two samples. In both samples, a vortex glass region with zero electrical resistance and a vortex liquid region with a finite electrical resistance value were observed. This vortex liquid region is further divided into a critical region, a pinned vortex liquid region, and an unpinned vortex liquid region. The critical region has a large activation energy due to the development of vortex glass, and the activation energy is expressed as $U_{eff} = k_B T(T_c - T)/(T_c - T_g)$. Meanwhile, the pinned vortex liquid region is described by the thermally activated flux motion (TAFM) with an activation energy $U(T,B) = U_0(B)(1-t)^q$ that is nonlinearly dependent on temperature. In the unpinned vortex liquid region, there is no restriction on the flux motion due to the activation energy that is small compared to temperature. The magnetic field dependence of the zero-temperature activation energy in the $B//c$ direction determined by TAFM motion in the pinned vortex liquid region shows the form of $U_0(B) \sim B^{-\alpha}$ with $\alpha = 1.21$ −1.22 due to the entanglement of flux lines strongly pinned to point defects in both pristine and irradiated samples. On the other hand, $U_0(B)$ for both samples in the direction of $B//ab$ increases significantly over the entire measured magnetic field region compared to that in $B//c$, and decreases nonlinearly with respect to magnetic field changes at high magnetic fields. This is due to the vortex pinned from the long normal-like state region

formed along the *c*-axis direction by the short coherent length ξ_c.

Author statement

Y.S.K. designed the research. W.J.C. and Y.I.S. performed single crystal growth, proton irradiation, X-ray diffraction, electron diffraction, and magnetoresistivity experiments. K.P. helped in data interpretation and analysis. Y.S.K, W.J.C. and Y.I.S. wrote this manuscript.

Declaration of Competing Interest

The authors declare that they have no known competing financial interests or personal relationships that could have appeared to influence the work reported in this paper.

Acknowledgements

References

[1] Huse DA, Fisher MPA, Fisher DS. Are superconductors really superconducting? Nature 1992;358(6387):553–9. https://doi.org/10.1038/358553a0.

[2] Dai P. Antiferromagnetic order and spin dynamics in iron-based superconductors. Rev Mod Phys 2015;87(3):855–96. https://doi.org/10.1103/RevModPhys.87.855.

[3] Kalisky B, Kirtley JR, Analytis JG, Chu JH, Fisher IR, Moler KA. Behavior of vortices near twin boundaries in underdoped Ba(Fe$_{1-x}$Co$_x$)$_2$As$_2$. Phys Rev B 2011; 83:064511. https://doi.org/10.1103/PhysRevB.83.064511.

[4] Hänisch J, Iida K, Kurth F, Reich E, Tarantini C, Jaroszynski J, et al. High field superconducting properties of Ba(Fe$_{1-x}$Co$_x$)$_2$As$_2$ thin films. Sci Rep 2015;5(1): 17363. https://doi.org/10.1038/srep17363.

[5] Iida K, Hänisch J, Yamamoto A. Grain boundary characteristics of Fe-based superconductors. Supercond Sci Technol 2020;33(4):043001. https://doi.org/10.1088/1361-6668/ab73ef.

[6] Reichhardt C, Olson Reichhardt CJ. Depinning and nonequilibrium dynamic phases of particle assemblies driven over random and ordered substrates: a review. Reports Prog Phys 2017;80(2):026501. https://doi.org/10.1088/1361-6633/80/2/026501.

[7] Kwok W-K, Welp U, Glatz A, Koshelev AE, Kihlstrom KJ, Crabtree GW. Vortices in high-performance high-temperature superconductors. Rep Prog Phys 2016;79(11): 116501. https://doi.org/10.1088/0034-4885/79/11/116501.

[8] Mizukami Y, Konczykowski M, Kawamoto Y, Kurata S, Kasahara S, Hashimoto K, et al. Disorder-induced topological change of the superconducting gap structure in iron pnictides. Nat Commun 2014;5(1):5657. https://doi.org/10.1038/ncomms6657.

[9] Eisterer M. Radiation effects on iron-based superconductors. Supercond Sci Technol 2018;31(1):013001. https://doi.org/10.1088/1361-6668/aa9882.

[10] Roas B, Schultz L, Saemann-Ischenko G. Anisotropy of the critical current density in epitaxial YBa$_2$Cu$_3$O$_x$ films. Phys Rev Lett 1990;64:479–82. https://doi.org/10.1103/PhysRevLett.64.479.

[11] Schmitt P, Kummeth P, Schultz L, Saemann-Ischenko G. Two-dimensional behavior and critical-current anisotropy in epitaxial Bi$_2$Sr$_2$CaCu$_2$O$_{8+x}$ thin films. Phys Rev Lett 1991;67:267–70. https://doi.org/10.1103/PhysRevLett.67.267.

[12] Yamasaki H, Endo K, Kosaka S, Umeda M, Yoshida S, Kajimura K. Scaling of the flux pinning force in epitaxial Bi$_2$Sr$_2$Ca$_2$Cu$_3$O$_x$ thin films. Phys Rev Lett 1993;70: 3331–4. https://doi.org/10.1103/PhysRevLett.70.3331.

[13] Gao ZX, Osquiguil E, Maenhoudt M, Wuyts B, Libbrecht S, Bruynseraede Y. 3D–2D dimensional crossover in YBa$_2$Cu$_3$O$_7$ films. Phys Rev Lett 1993;71:3210–3. https://doi.org/10.1103/PhysRevLett.71.3210.

[14] Tachiki M, Takahashi S. Strong vortex pinning intrinsic in high-T_c oxide superconductors. Solid State Commun 1989;70(3):291–5. https://doi.org/10.1016/0038-1098(89)90330-X.

[15] Ivlev BI, Kopnin NB. Vortex motion in high-T_c superconductors near the upper critical field H_{c2}. J Low Temp Phys 1989;77(5-6):413–27. https://doi.org/10.1007/BF00682753.

[16] Feinberg D, Villard C. Intrinsic pinning and lock-in transition of flux lines in layered type-II superconductors. Phys Rev Lett 1990;65(7):919–22. https://doi.org/10.1103/PhysRevLett.65.919.

[17] Chakravarty S, Ivlev BI, Ovchinnikov YN. Resistivity of high-temperature superconductors: Is the vortex state a liquid? Phys Rev Lett 1990;64(26):3187–90. https://doi.org/10.1103/PhysRevLett.64.3187.

[18] Tachiki M, Takahashi S, Sunaga K. Driving and pinning forces acting on vortices in layered superconductors. Phys Rev B 1993;47(10):6095–105. https://doi.org/10.1103/PhysRevB.47.6095.

[19] Stürzer T, Stürzer C, Johrendt D. Iron arsenide superconductors (CaFeAs)$_{10}$M$_n$As$_8$ with metallic interlayers (M = Pt, Pd; n = 3, 4). Phys Status Solidi B 2017;254: 1600417. https://doi.org/10.1002/pssb.201600417.

[20] Stürzer T, Derondeau G, Bertschler EM, Johrendt D. Superconductivity by rare earth doping in the 1038-type compounds (Ca$_{1-x}$RE$_x$)$_{10}$(FeAs)$_{10}$(Pt$_3$As$_8$) with RE=Y, La-Nd, Sm-Lu. Solid State Commun 2015;201:36–9. https://doi.org/10.1016/j.ssc.2014.10.007.

[21] Xiang ZJ, Luo XG, Ying JJ, Wang XF, Yan YJ, Wang AF, et al. Transport properties and electronic phase diagram of single-crystalline Ca$_{10}$(Pt$_3$As$_8$)((Fe$_{1-x}$Pt$_x$)$_2$As$_2$)$_5$. Phys Rev B 2012;85:224527. https://doi.org/10.1103/PhysRevB.85.224527.

[22] Neupane M, Liu C, Xu SY, Wang YJ, Ni N, Allred JM, et al. Fermi-surface topology and low-lying electronic structure of the iron-based superconductor Ca$_{10}$(Pt$_3$As$_8$)(Fe$_2$As$_2$)$_5$. Phys Rev B 2012;85:094510. https://doi.org/10.1103/PhysRevB.85.094510.

[23] Ni N, Allred JM, Chan BC, Cava RJ. High T_c electron doped Ca$_{10}$(Pt$_3$As$_8$)(Fe$_2$As$_2$)$_5$ and Ca$_{10}$(Pt$_4$As$_8$)(Fe$_2$As$_2$)$_5$ superconductors with skutterudite intermediary layers. PNAS 2011;108(45):E1019–26. https://doi.org/10.1073/pnas.1110563108.

[24] Damascelli A, Hussain Z, Shen Z-X. Angle-resolved photoemission studies of the cuprate superconductors. Rev Mod Phys 2003;75(2):473–541. https://doi.org/10.1103/RevModPhys.75.473.

[25] Sterne PA, Wang CS. Higher T_c through metallic inter-layer coupling in Bi$_2$Sr$_2$CaCu$_2$O$_8$. J Phys C Solid State Phys 1988;21(26):L949–55. https://doi.org/10.1088/0022-3719/21/26/005.

[26] Sheng ZZ, Hermann AM, El Ali A, Almasan C, Estrada J, Datta T, et al. Superconductivity at 90 K in the Tl-Ba-Cu-O system. Phys Rev Lett 1988;60(10): 937–40. https://doi.org/10.1103/PhysRevLett.60.937.

[27] Parkin SSP, Lee VY, Engler EM, Nazzal AI, Huang TC, Gorman G, et al. Bulk superconductivity at 125 K in Tl$_2$Ca$_2$Ba$_2$Cu$_3$O$_x$. Phys Rev Lett 1988;60:2539. https://doi.org/10.1103/PhysRevLett.60.2539.

[28] Ni N, Straszheim WE, Williams DJ, Tanatar MA, Prozorov R, Bauer ED, et al. Transport and thermodynamic properties of (Ca$_{1-x}$La$_x$)$_{10}$(Pt$_3$As$_8$)(Fe$_2$As$_2$)$_5$ superconductors. Phys Rev B 2013;87:060507(R). https://doi.org/10.1103/PhysRevB.87.060507.

[29] Thirupathaiah S, Stürzer T, Zabolotnyy VB, Johrendt D, Büchner B, Borisenko SV. Why T_c of (CaFeAs)$_{10}$Pt$_{3.58}$As$_8$ is twice as high as (CaFeAs)$_{10}$Pt$_{0.05}$As$_8$. Phys Rev B 2013;88:140505(R). https://doi.org/10.1103/PhysRevB.88.140505.

[30] Gao P, Sun L, Ni Ni, Guo J, Wu Qi, Zhang C, et al. Pressure-induced superconductivity and its scaling with doping-induced superconductivity in the iron pnictide with skutterudite intermediary layers. Adv Mater 2014;26(15): 2346–51. https://doi.org/10.1002/adma.v26.15.10.1002/adma.201305154.

[31] Seo YI, Choi WJ, Kimura SI, Bang Y, Kwon YS. Optical properties of optimally doped single-crystal Ca$_{8.5}$La$_{1.5}$(Pt$_3$As$_8$)(Fe$_2$As$_2$)$_5$. Phys Rev B 2017;95:094510. https://doi.org/10.1103/PhysRevB.95.094510.

[32] Seo Y-i, Choi W-J, Ahmad D, Kimura S-I, Kwon YS. Temperature dependence of the superconducting energy gaps in Ca$_{9.35}$La$_{0.65}$(Pt$_3$As$_8$)(Fe$_2$As$_2$)$_5$ single crystal. Sci Rep 2018;8(1):8648. https://doi.org/10.1038/s41598-018-24940-9.

[33] Yang R, Dai Y, Yu J, Sui Q, Cai Y, Ren Z, et al. Unravelling the mechanism of the semiconducting-like behavior and its relation to superconductivity in (CaFe$_{1-x}$Pt$_x$As)$_{10}$Pt$_3$As$_8$. Phys Rev B 2019;99:144520. https://doi.org/10.1103/PhysRevB.99.144520.

[34] Watson MD, McCollam A, Blake SF, Vignolles D, Drigo L, Mazin II, et al. Field-induced magnetic transitions in Ca$_{10}$(Pt$_3$As$_8$)((Fe$_{1-x}$Pt$_x$)$_2$As$_2$)$_5$ compounds. Phys Rev B 2014;89:205136. https://doi.org/10.1103/PhysRevB.89.205136.

[35] Kim J, Ronning F, Haberkorn N, Civale L, Nazaretski E, Ni N, et al. Large magnetic penetration depth and thermal fluctuations in a superconducting Ca$_{10}$(Pt$_3$As$_8$)[(Fe$_{1-x}$Pt$_x$)$_2$As$_2$]$_5$ (x = 0.097) single crystal. Phys Rev B 2012;85:180504(R). https://doi.org/10.1103/PhysRevB.85.180504.

[36] Cho K, Tanatar MA, Kim H, Straszheim WE, Ni N, Cava RJ, et al. Doping-dependent superconducting gap anisotropy in the two-dimensional pnictide Ca$_{10}$(Pt$_3$As$_8$)[(Fe$_{1-x}$Pt$_x$)$_2$As$_2$]$_5$. Phys Rev B 2012;85:020504(R). https://doi.org/10.1103/PhysRevB.85.020504.

[37] Choi WJ, Seo YI, Ahmad D, Kwon YS. Thermally activated flux motion in optimally electron-doped (Ca$_{0.85}$La$_{0.15}$)$_{10}$(Pt$_3$As$_8$)(Fe$_2$As$_2$)$_5$ and Ca$_{10}$(Pt$_3$As$_8$)((Fe$_{0.92}$Pt$_{0.08}$)$_2$As$_2$)$_5$ single crystals. Results Phys 2020;19:103430. https://doi.org/10.1016/j.rinp.2020.103430.

[38] Ziegler JF, Biersack JP, Littmark U. SRIM-The Stopping and Range of Ions in Solids. Pergamon 1985. http://www.srim.org.

[39] Y. Seto. Crystallography Software ReciPro. https://pmsl.planet.sci.kobe-u.ac.jp/~seto/.

[40] Stürzer T, Derondeau G, Johrendt D. Role of different negatively charged layers in Ca$_{10}$(FeAs)$_{10}$(Pt$_4$As$_8$) and superconductivity at 30 K in electron-doped (Ca$_{0.8}$La$_{0.2}$)$_{10}$(FeAs)$_{10}$(Pt$_3$As$_8$). Phys Rev B 2012;86:060516(R). https://doi.org/10.1103/PhysRevB.86.060516.

[41] Wang Z, Jin R, Wu L, Tao J, Karki AB, Pan JY, et al. Atomically imaged crystal structure and normal-state properties of superconducting Ca$_{10}$Pt$_4$As$_8$((Fe$_{1-x}$Pt$_x$)$_2$As$_2$)$_5$. Phys Rev B 2019;100:94103. https://doi.org/10.1103/PhysRevB.100.094103.

[42] Holland TJB, Redfern SAT. UNITCELL: a nonlinear least-squares program for cell-parameter refinement and implementing regression and deletion diagnostics. J Appl Crystallogr 1997;30(1):84. https://doi.org/10.1107/S0021889896011673.

[43] Kakiya S, Kudo K, Nishikubo Y, Oku K, Nishibori E, Sawa H, et al. Superconductivity at 38 K in Iron-Based Compound with Platinum-Arsenide Layers Ca$_{10}$(Pt$_4$As$_8$)(Fe$_{2-x}$Pt$_x$As$_2$)$_5$. J Phys Soc Japan 2011;80(9):093704. https://doi.org/10.1143/JPSJ.80.093704.

[44] Kim J, Haberkorn N, Graf MJ, Usov I, Ronning F, Civale L, et al. Magnetic penetration-depth measurements of a suppressed superfluid density of

superconducting $Ca_{0.5}Na_{0.5}Fe_2As_2$ single crystals by proton irradiation. Phys Rev B 2012;86:144509. https://doi.org/10.1103/PhysRevB.86.144509.

[45] Bulaevskil LN, Guselnov AA, Rusinov AI. Superconductivity in crystals without symmetry centers. Sov Phys JETP 1977;44:1243–51.

[46] Putti M, Affronte M, Ferdeghini C, Manfrinetti P, Tarantini C, Lehmann E. Observation of the crossover from two-gap to single-gap superconductivity through specific heat measurements in neutron-irradiated MgB_2. Phys Rev Lett 2006;96: 077003. https://doi.org/10.1103/PhysRevLett.96.077003.

[47] Efremov DV, Korshunov MM, Dolgov OV, Golubov AA, Hirschfeld PJ. Disorder-induced transition between $s_\pm$ and s_{++} states in two-band superconductors. Phys Rev B 2011;84:180512(R). https://doi.org/10.1103/PhysRevB.84.180512.

[48] Wang Y, Kreisel A, Hirschfeld PJ, Mishra V. Using controlled disorder to distinguish $s_\pm$ and s_{++} gap structure in Fe-based superconductors. Phys Rev B 2013;87:094504. https://doi.org/10.1103/PhysRevB.87.094504.

[49] Cho K, Kończykowski M, Murphy J, Kim H, Tanatar MA, Straszheim WE, et al. Effects of electron irradiation on resistivity and London penetration depth of $Ba_{1-x}K_xFe_2As_2$ ($x \leq 0.34$) iron-pnictide superconductor. Phys Rev B 2014;90:104514. https://doi.org/10.1103/PhysRevB.90.104514.

[50] Strehlow CP, Kończykowski M, Murphy JA, Teknowijoyo S, Cho K, Tanatar MA, et al. Comparative study of the effects of electron irradiation and natural disorder in single crystals of $SrFe_2(As_{1-x}P_x)_2$ superconductor ($x = 0.35$). Phys Rev B 2014; 90:020508(R). https://doi.org/10.1103/PhysRevB.90.020508.

[51] López D, Krusin-Elbaum L, Safar H, Righi E, de la Cruz F, Grigera S, et al. Pinned vortex liquid above the critical point of the first-order melting transition: a consequence of pointlike disorder. Phys Rev Lett 1998;80(5):1070–3. https://doi.org/10.1103/PhysRevLett.80.1070.

[52] Ahmad D, Seo YI, Choi WJ, Kwon YS. Fluctuation-induced magnetoconductivity in pristine and proton-irradiated $Ca_{8.5}La_{1.5}(Pt_3As_8)(Fe_2As_2)_5$ single crystals. Supercond Sci Technol 2017;30(2):025009. https://doi.org/10.1088/1361-6668/30/2/025009.

[53] Stürzer T, Kessler F, Johrendt D. Superconductivity by transition metal doping in $Ca_{10}(Fe_{1-x}M_xAs)_{10}(Pt_3As_8)$ (M = Co, Ni, Cu). Philos Mag 2014;94(31):3632–9. https://doi.org/10.1080/14786435.2014.966796.

[54] Löhnert C, Stürzer T, Tegel M, Frankovsky R, Friederichs G, Johrendt D. Superconductivity up to 35 K in the iron platinum arsenides $(CaFe_{1-x}Pt_xAs)_{10}Pt_{4-y}As_8$ with layered structures. Angew Chem Int Ed 2011;50:9195–9. https://doi.org/10.1002/anie.201104436.

[55] Ernst S, Kirchner S, Krellner C, Geibel C, Zwicknagl G, Steglich F, et al. Emerging local Kondo screening and spatial coherence in the heavy-fermion metal $YbRh_2Si_2$. Nature 2011;474(7351):362–6. https://doi.org/10.1038/nature10148.

[56] Blatter G, Feigel'man MV, Geshkenbein VB, Larkin AI, Vinokur VM. Vortices in high-temperature superconductors. Rev Mod Phys 1994;66(4):1125–388. https://doi.org/10.1103/RevModPhys.66.1125.

[57] Palstra TTM, Batlogg B, Schneemeyer LF, Waszczak JV. Thermally Activated Dissipation in $Bi_{2.2}Sr_2Ca_{0.8}Cu_2O_{8+\delta}$. Phys Rev Lett 1988;61:1662–5. https://doi.org/10.1103/PhysRevLett.61.1662.

[58] Zhang YZ, Wen HH, Wang Z. Thermally activated energies of $YBa_2Cu_3O_{7-\delta}$ and $Y_0Ca_{0.2}Ba_2Cu_3O_{7-\delta}$ thin films. Phys Rev B 2006;74:144521. https://doi.org/10.1103/PhysRevB.74.144521.

[59] Zhang YZ, Ren ZA, Zhao ZX. Thermally activated energy and critical magnetic fields of $SmFeAsO_{0.9}F_{0.1}$. Supercond Sci Technol 2009;22(6):065012. https://doi.org/10.1088/0953-2048/22/6/065012.

[60] Nakajima Y, Tsuchiya Y, Taen T, Tamegai T, Okayasu S, Sasase M. Enhancement of critical current density in Co-doped $BaFe_2As_2$ with columnar defects introduced by heavy-ion irradiation. Phys Rev B 2009;80:012510. https://doi.org/10.1103/PhysRevB.80.012510.

[61] Shabbir B, Wang X, Ghorbani SR, Wang AF, Dou S, Chen XH. Giant enhancement in critical current density, up to a hundredfold, in superconducting $NaFe_{0.97}Co_{0.03}As$

single crystals under hydrostatic pressure. Sci Rep 2015;5(1):10606. https://doi.org/10.1038/srep10606.

[62] Fisher MPA. Vortex-glass superconductivity: a possible new phase in bulk High-T_c oxides. Phys Rev Lett 1989;62:1415. https://doi.org/10.1103/PhysRevLett.62.1415.

[63] Liu SL, Wu GJ, Xu XB, Wu J, Shao HM. Scaling of the vortex-liquid resistivity in high temperature superconductors. Supercond Sci Technol 2005;18(10):1332–6. https://doi.org/10.1088/0953-2048/18/10/014.

[64] Abulafia Y, Shaulov A, Wolfus Y, Prozorov R, Burlachkov L, Yeshurun Y, et al. Plastic vortex creep in $YBa_2Cu_3O_{7-x}$ crystals. Phys Rev Lett 1996;77:1596–9. https://doi.org/10.1103/PhysRevLett.77.1596.

[65] Küpfer H, Gordeev SN, Jahn W, Kresse R, Meier-Hirmer R, Wolf T, et al. Phase diagram of flux creep in melt-textured and single-crystalline $YBa_2Cu_3O_{7-\delta}$. Phys Rev B 1994;50:7016–25. https://doi.org/10.1103/PhysRevB.50.7016.

[66] Geshkenbein V, Larkin A, Feigel'man M, Vinokur V. Flux pinning and creep in high-T_c superconductors. Phys C Supercond Its Appl 1989;162-164:239–40. https://doi.org/10.1016/0921-4534(89)91006-X.

[67] V. M. Vinokur, M. V. Feigel'man, V. B. Geshkenbein and AIL. Resistivity of high-superconductors in a vortex-liquid state. Phys Rev Lett 1990;65:259–62. doi: 10.1103/PhysRevLett.65.259.

[68] Kierfeld J, Nordborg H, Vinokur VM. Theory of plastic vortex creep. Phys Rev Lett 2000;85(23):4948–51. https://doi.org/10.1103/PhysRevLett.85.4948.

[69] Fente A, Meier WR, Kong T, Kogan VG, Bud'Ko SL, Canfield PC, et al. Influence of multiband sign-changing superconductivity on vortex cores and vortex pinning in stoichiometric high-T_c $CaKFe_4As_4$. Phys Rev B 2018;97:134501. https://doi.org/10.1103/PhysRevB.97.134501.

[70] Torsello D, Ummarino GA, Bekaert J, Gozzelino L, Gerbaldo R, Tanatar MA, et al. Tuning the intrinsic anisotropy with disorder in the $CaKFe_4As_4$ superconductor. Phys Rev Appl 2020;13:064046. https://doi.org/10.1103/PhysRevApplied.13.064046.

[71] Reichhardt C, van Otterlo A, Zimányi GT. Vortices freeze like window glass: the vortex molasses scenario. Phys Rev Lett 2000;84(9):1994–7. https://doi.org/10.1103/PhysRevLett.84.1994.

[72] Fischer KH. Vortices in high-T_c superconductors. Supercond Rev 1995;1:153.

[73] Shan L, Yau JKF, Jin X, Lu RT, Fang L, He M, et al. Anisotropic phase diagram at higher temperature for $Tl_2Ba_2CaCu_2O_8$ thin film. Supercond Sci Technol 2001;14 (7):457–62. https://doi.org/10.1088/0953-2048/14/7/307.

[74] Wang X-L, Ghorbani SR, Lee S-I, Dou SX, Lin CT, Johansen TH, et al. Very strong intrinsic flux pinning and vortex avalanches in $(Ba, K)Fe_2As_2$ superconducting single crystals. Phys Rev B 2010;82:024525. https://doi.org/10.1103/PhysRevB.82.024525.

[75] Xing XZ, Li ZF, Yi XL, Feng JJ, Xu CQ, Zhou N, et al. Thermally activated flux flow, vortex-glass phase transition and the mixed-state Hall effect in 112-type iron pnictide superconductors. Sci China-Phys Mech Astron 2018;61(12):127406. https://doi.org/10.1007/s11433-018-9280-6.

[76] Zhou W, Zhuang J, Yuan F, Li X, Xing X, Sun Y, et al. Anisotropic superconductivity of $Ca_{1-x}La_xFeAs_2$ ($x \sim 0.18$) single crystal. Appl Phys Express 2014;7:063102. https://doi.org/10.7567/APEX.7.063102.

[77] Lee HS, Bartkowiak M, Kim JS, Lee HJ. Magnetic-field-induced crossover of vortex-line coupling in $SmFeAsO_{0.85}$ single crystal. Phys Rev B 2010;82:104523. https://doi.org/10.1103/PhysRevB.82.104523.

[78] Prando G, Carretta P, De Renzi R, Sanna S, Palenzona A, Putti M, et al. Vortex dynamics and irreversibility line in optimally doped $SmFeAsO_{0.8}F_{0.2}$ from ac susceptibility and magnetization measurements. Phys Rev B 2011;83:174514. https://doi.org/10.1103/PhysRevB.83.174514.

[79] Jiao L, Kohama Y, Zhang JL, Wang HD, Maiorov B, Balakirev FF, et al. Upper critical field and thermally activated flux flow in single-crystalline $Tl_{0.58}Rb_{0.42}Fe_{1.72}Se_2$. Phys Rev B 2012;85:064513. https://doi.org/10.1103/PhysRevB.85.064513.